JACS
JOURNAL OF THE AMERICAN CHEMICAL SOCIETY
pubs.acs.org/JACS
Article

Synthetic Control of Exciton Dynamics in Bioinspired Cofacial Porphyrin Dimers

Partha Pratim Roy, Sohang Kundu, Jesús Valdiviezo, George Bullard, James T. Fletcher, Rui Liu, Shiun-Jr Yang, Peng Zhang, David N. Beratan, Michael J. Therien, Nancy Makri,* and Graham R. Fleming*

Cite This: *J. Am. Chem. Soc.* 2022, 144, 6298–6310

Read Online

ACCESS | Metrics & More | Article Recommendations | Supporting Information

ABSTRACT: Understanding how the complex interplay among excitonic interactions, vibronic couplings, and reorganization energy determines coherence-enabled transport mechanisms is a grand challenge with both foundational implications and potential payoffs for energy science. We use a combined experimental and theoretical approach to show how a modest change in structure may be used to modify the exciton delocalization, tune electronic and vibrational coherences, and alter the mechanism of exciton transfer in covalently linked cofacial Zn-porphyrin dimers (*meso-beta* linked $AB_{m\text{-}\beta}$ and *meso*−*meso* linked $AA_{m\text{-}m}$). While both $AB_{m\text{-}\beta}$ and $AA_{m\text{-}m}$ feature zinc porphyrins linked by a 1,2-phenylene bridge, differences in the interporphyrin connectivity set the lateral shift between macrocycles, reducing electronic coupling in $AB_{m\text{-}\beta}$ and resulting in a localized exciton. Pump−probe experiments show that the exciton dynamics is faster by almost an order of magnitude in the strongly coupled $AA_{m\text{-}m}$ dimer, and two-dimensional electronic spectroscopy (2DES) identifies a vibronic coherence that is absent in $AB_{m\text{-}\beta}$. Theoretical studies indicate how the interchromophore interactions in these structures, and their system-bath couplings, influence excitonic delocalization and vibronic coherence-enabled rapid exciton transport dynamics. Real-time path integral calculations reproduce the exciton transfer kinetics observed experimentally and find that the linking-modulated exciton delocalization strongly enhances the contribution of vibronic coherences to the exciton transfer mechanism, and that this coherence accelerates the exciton transfer dynamics. These benchmark molecular design, 2DES, and theoretical studies provide a foundation for directed explorations of nonclassical effects on exciton dynamics in multiporphyrin assemblies.

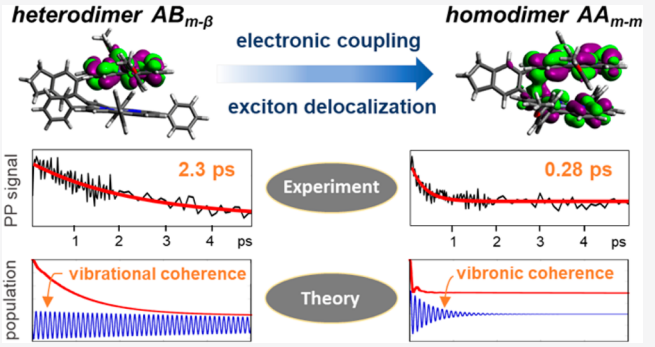

INTRODUCTION

Electronically coupled arrays of chromophores[1−3] offer the tantalizing prospect of directing energy or charge flow over large distances, mimicking natural light harvesting systems. The aim of this experimental−theoretical study is to examine the interplay among structure, exciton delocalization, reorganization energy and vibronic effects on exciton transport and dynamics,[4,5] with the goal of developing strategies to exploit these parameters to control energy transfer and transport. For synthetic coherent transport systems, the optimal values of, and relations among, a number of key electronic and vibrational parameters need to be established.[6−9] The diverse roles of individual and collective vibrations in excitation energy transfer were recently identified and illustrated through fully quantum mechanical, all-mode path integral calculations in small and large molecular aggregates.[10] As a first step toward creating guidelines for functional synthetic structures, model systems are needed to explore the influence of molecular topology and symmetry on electronic mixing and vibronic coupling.[11−13] Studies of natural systems show that rapid coherent transport occurs when the electronic coupling and the reorganization energy are of similar magnitude.[14,15] For moderate interpigment electronic couplings (100−200 cm^{-1}), the reorganization energy should be in the 100−200 cm^{-1} range to achieve coherent transport.

Cofacial porphyrin systems realized through sequential metal catalyzed cross-coupling and cycloaddition reactions enable straightforward control of porphyrin−porphyrin lateral shift, the extent of porphyrin−porphyrin electronic asymmetry, and the nature of porphyrin−porphyrin topological connectivity, while maintaining a uniform 1,2-phenylene bridging motif.[16−18] These compositions define attractive platforms for exploring the landscape described above with modern

Received: December 7, 2021
Published: March 30, 2022

https://doi.org/10.1021/jacs.1c12889
J. Am. Chem. Soc. 2022, 144, 6298−6310

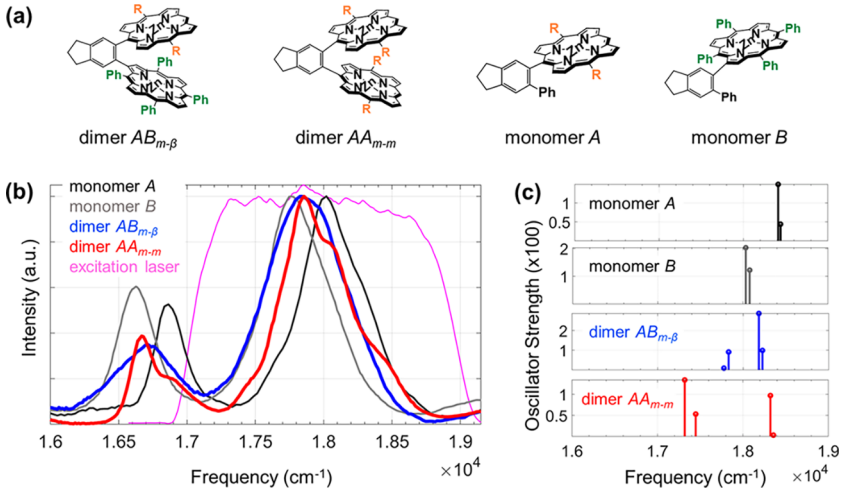

Figure 1. (a) Chemical structures of cofacially linked zinc porphyrin dimers $AB_{m-\beta}$ and AA_{m-m}, and the constituent monomers *A* and *B*. R = 4-(3-methoxy-3-methylbutoxy)phenyl; Ph = phenyl. (b) Normalized linear absorption spectra of dimers $AB_{m-\beta}$, $AA_{m\ m}$ and monomers *A*, *B* in the visible Q-band region at 95 K in 3:1 diethyl ether/ethanol are shown by blue, red, black and gray curves, respectively. In each compound, two bands are denoted as Q (0−0) and Q (0−1). The magenta curve shows the laser excitation spectrum used for the experiments. (c) Oscillator strengths and vertical transition frequencies of the Q-band absorptions present in monomers (*A*, *B*) and dimers ($AB_{m-\beta}$, AA_{m-m}) obtained from TDDFT calculations at the CAM-B3LYP-D3(BJ)/def2-SVP level of theory, which only refer to the electronic component, i.e. Q (0−0) transition.

multidimensional spectroscopies[19−24] combined with electronic structure and path integral quantum dynamical calculations.[25−27] Such rigid, face-to-face bis(porphyrin) structures provide opportunities to extensively regulate the scope of interporphyryl $\pi-\pi$ interactions and the magnitude of porphyrin−porphyrin electronic and excitonic coupling,[16−18] and probe critical structure−function relationships that inform our understanding of and ability to manipulate coherence in electronically coupled, vibronically mixed multichromophore arrays. In this paper we examine two such dimers (Figure 1a) and use a combination of two-dimensional electronic spectroscopy (2DES), electronic structure calculations, and path integral dynamics calculations to illuminate how differences in porphyrin−porphyrin electronic coupling and porphyrin−porphyrin lateral shift and symmetry impact coherent exciton dynamics.

RESULTS AND DISCUSSION

Absorption Spectra and Electronic Structure. *Electronic Spectra of Porphyrin Monomers and Dimers.* The linear absorption spectra are shown in Figure 1b in a 3:1 mixture of diethyl ether and ethanol for the monomers (*A* and *B*) and the two dimers ($AB_{m-\beta}$ and AA_{m-m}) where the subscript *m-β* denotes a *meso-beta* linkage and *m-m* denotes a *meso−meso* linkage. Porphyrin spectra typically contain a very intense band in the vis-spectral region (~24 000 cm^{-1}), known as the Soret or B-band, and a pair of weaker bands (Q 0−0 and 0−1 bands) at lower energy (14 000−21 000 cm^{-1}). These electronic transitions are readily understood by Gouterman's four orbital model,[28,29] which involves a degenerate pair of LUMOs (e_g) and a nearly degenerate pair of HOMOs (a_{1u} and a_{2u}). The large interaction between the two lowest energy orbital excitations causes the transition dipoles to add and form a pair of intense B-bands (B_x and B_y); the excitations nearly cancel out to form a nearly degenerate pair of weaker Q (0−0) bands (Q_x and Q_y). In the porphyrin monomers *A* and *B*, substitution of the meso and *β* positions breaks the symmetry, lifts the degeneracy of Q_x and Q_y transitions, and produces differing oscillator strengths (Figure 1c).

Significant intensity is regained in the Q-transition through Herzberg−Teller (HT) vibronic mixing[30] with the B-transitions to produce the Q (0−1) bands.[31,32] The absorption spectra of monomeric metalloporphyrin complexes in the visible Q-band region were recently discussed in detail.[33−36] The Q-band is derived from numerous modes in the low frequency band and numerous 0−1 transitions (600−1500 cm^{-1}) among HT active modes in the higher frequency peak. For notational convenience, we will refer to the two main peaks as 0−0 and 0−1 (Figure 1b). The spectra of the dimers are rather similar to those of the monomers, although the relative intensity of the 0−0 band compared to the 0−1 band is reduced for the dimer in both cases. The lowest energy excited state is doubly degenerate in a fully symmetric (D_{4h}) monomer;[28,29,37] for monomers *A* and *B* (Figure 1a), the splitting of the Q-band into Q_x and Q_y transitions is very small and is masked by spectral broadening and congestion. In the dimers, then, we expect four excitonic states; the calculated oscillator strength to 0−0 band states (at the CAM-B3LYP-D3(BJ)/def2-SVP level[38−40] including THF with the PCM implicit solvation model[41]) varies from smallest to largest by a factor of almost 50 for the ground-to-excitonic state transitions for AA_{m-m} and by a factor of 30 for $AB_{m-\beta}$ (Figure 1c). Note that the calculated oscillator strengths are obtained within the Franck−Condon approximation. The greater spectral width of both dimers compared to the monomers, and the prominent shoulder (~200 cm^{-1} to the blue of the peak maximum) on the 0−0 and 0−1 bands of dimer AA_{m-m} suggests the presence of at least two excitonic transitions with an energy gap of ~200 cm^{-1} (Figure 1b). While conformational heterogeneity plays a role in the spectral broadening of covalently linked multiporphyrin compounds,[42] we note that, for these cofacial porphyrin structures linked by a 1,2-phenylene-bridge, the extent of conformational heterogeneity is highly restricted.[16−18,43,44] In both dimers, the calculated energies of the excitons split into two groups of two (Figure 1c), giving rise to the prominent shoulder peak on both 0−0 and 0−1 bands of dimer AA_{m-m}. A second shoulder at ~18 400 cm^{-1} is also apparent on the 0−1 band. No such doublet excitonic

https://doi.org/10.1021/jacs.1c12889
J. Am. Chem. Soc. 2022, 144, 6298−6310

peaks are observed in the linear spectrum of dimer $AB_{m\text{-}\beta}$ mainly because of much smaller excitonic splitting (Figure 1c). In addition, the large disparity in oscillator strengths between two exciton pairs (Figure 1c) may cause the high frequency excitonic transition pair to remain buried under the intense, lower frequency excitonic transition pair.

Comparison of Electronic Coupling and Exciton Delocalization. To explore the influence of the structure and linkage topology on the electronic states and coupling in the dimers, we ran geometry optimization (optimized molecular coordinates in Table S6−S8 in the Supporting Information) and vibrational frequency analysis employing density functional theory (DFT) calculations at the CAM-B3LYP-D3(BJ)/def2-SVP level[38−40] as implemented in Gaussian 16.[45] Similar results were found with the MN15 functional[46] (in Gaussian 16[45]) and with CC2 theory[47] (in TURBOMOLE)[48] (Table S1). We used a PCM model[41] for tetrahydrofuran to match the dielectric constant of the 3:1 diethyl ether and ethanol mixtures used to make the glass. The calculations for the monomer agree with earlier studies that found the Q_x and Q_y transitions to be nearly degenerate.[28,29,36,37] The vertical transition energies for both monomers and dimers are overestimated by ∼1500 cm^{-1} (Figure 1c) compared to the experimental value (0−0 peak), which is typical for this level of theory.[49] We note that the calculated excitation energy contains a contribution from the vibrational reorganization energy. However, based on the small Stokes shift in fluorescence (see Figure S1 in Supporting Information), the reorganization energy is smaller than 100 cm^{-1}. Further, the calculated splitting of the two exciton pairs (S_1−S_3 and S_2−S_4) appears to be overestimated by a factor of 3−4 in comparison to the values suggested by the shoulders of the absorption spectra (Figure 1b). The overestimate of the coupling most likely arises from the neglect of Herzberg−Teller (HT) and HT-Franck−Condon interference.[50−53] Including these effects in the calculation of the couplings is certainly possible, but is beyond the scope of the current work. The current level of calculation is, however, extremely useful for qualitative guidance, and our dynamical calculations are based on couplings extracted from the experimental spectra. We now turn to more detailed discussion of the two dimers.

The natural transition orbitals (NTOs)[54] for the four vertical excitonic transitions, shown in the SI (Figure S2), are largely localized on one monomer in $AB_{m\text{-}\beta}$, while in $AA_{m\text{-}m}$ the NTOs are delocalized over both monomeric units. A complementary perspective is offered by the electronic coupling between the diabatic states calculated in Q-Chem 5.3.2 using the fragment-excitation difference (FED) method[55,56] at the CAM-B3LYP-D3(BJ)/def2-SVP level of theory with implicit tetrahydrofuran solvent (PCM scheme).[41] The results appear in Table 1. Note that the FED method is based on a two-state approximation, and the derived couplings contain no relative phase information among the exciton pairs. The calculated values of coupling (and excitation energies) are found to be robust to the choice of basis sets, methods, and solvents (Tables S1−S5 in the Supporting Information). The largest couplings in $AB_{m\text{-}\beta}$ are in the 130−180 cm^{-1} range, while most are below 50 cm^{-1}. In $AA_{m\text{-}m}$, the four largest couplings range from 380 to 516 cm^{-1}. To clarify the origin of these differences in coupling, the same set of calculations was performed for a hypothetical $AA_{m\text{-}\beta}$ dimer (homodimer with *meso-beta* linkage as shown in Figure S3). Table 1 shows that the coupling is reduced in the $AB_{m\text{-}\beta}$ dimer by 2 to 5 times compared to the $AA_{m\text{-}m}$ dimer. The hypothetical $AA_{m\text{-}\beta}$ dimer has intermediate coupling values, which are closer, overall, to those of the $AB_{m\text{-}\beta}$ dimer. These computational results, which pinpoint differences in diabatic state couplings, mirror experimental data[16] that underscore the role played by the linkage topology to the 1,2-phenylene bridge in these cofacial porphyrin systems, as *m-β* connectivity introduces a macrocycle−macrocycle lateral shift and produces diminished porphyrin−porphyrin electronic couplings relative to those in the *m-m* cofacial dimer topology.

Table 1. Electronic Couplings (Absolute Values) of Cofacial Porphyrin Dimers Calculated Using the Fragment-Excitation Difference (FED) Method[52a]

States (diabatic)		dimer $AB_{m\text{-}\beta}$ coupling (cm^{-1})	dimer $AA_{m\text{-}m}$ coupling (cm^{-1})	dimer $AA_{m\text{-}\beta}$[b] (hypothetical) coupling (cm^{-1})
1	2	8	64	28
1	3	177	395	217
1	4	48	516	96
2	3	40	435	56
2	4	129	379	210
3	4	0	16	24

[a]The geometry used corresponds to the ground state minimum. [b]The chemical structure of hypothetical dimer $AA_{m\text{-}\beta}$ is shown in Figure S3 of the Supporting Information.

To study the effect of the linker in the electronic couplings, we calculated the couplings for the dimers fixed in the ground state geometry, but with the indane linker removed (Table 2).

Table 2. Electronic Couplings (Absolute Values) of Cofacial Porphyrin Dimers without the Indane Linker Unit Calculated Using the Fragment-Excitation Difference (FED) Method[52a]

States (diabatic)		dimer $AB_{m\text{-}\beta}$ (*without linker*) coupling (cm^{-1})	dimer $AA_{m\text{-}m}$ (*without linker*) coupling (cm^{-1})	dimer $AA_{m\text{-}\beta}$ (*without linker*) (hypothetical) coupling (cm^{-1})
1	2	8	78	32
1	3	241	96	298
1	4	64	750	258
2	3	81	621	202
2	4	233	120	305
3	4	8	16	8

[a]The geometry used corresponds to the ground state minimum.

Dangling bonds were capped with hydrogens. In all three cases, the coupling magnitudes of weakly coupled states were slightly larger than those of the covalently linked cases in Table 1, suggesting that the origin of the couplings in dimer $AB_{m\text{-}\beta}$ is through-space and that the through-bond interaction contributes an interference effect in dimer $AA_{m\text{-}m}$ that reduces the overall coupling. This finding is in line with an earlier report on π-stacked porphyrin−bridge−quinone systems.[57] On the other hand, removal of the indane linker decreased the values of V_{13} and V_{24} in dimer $AA_{m\text{-}m}$. Thus, in the Condon approximation, the linker weakens the electronic couplings. Note that the linker can also influence the transition dipole orientations and the extent of π−π orbital overlap. To complete the discussion of couplings it is helpful to return to the Q_x, Q_y picture of porphyrin optical transitions. In this context the small calculated couplings in each dimer correspond to Q_x − Q_y coupling as expected.

https://doi.org/10.1021/jacs.1c12889
J. Am. Chem. Soc. 2022, 144, 6298−6310

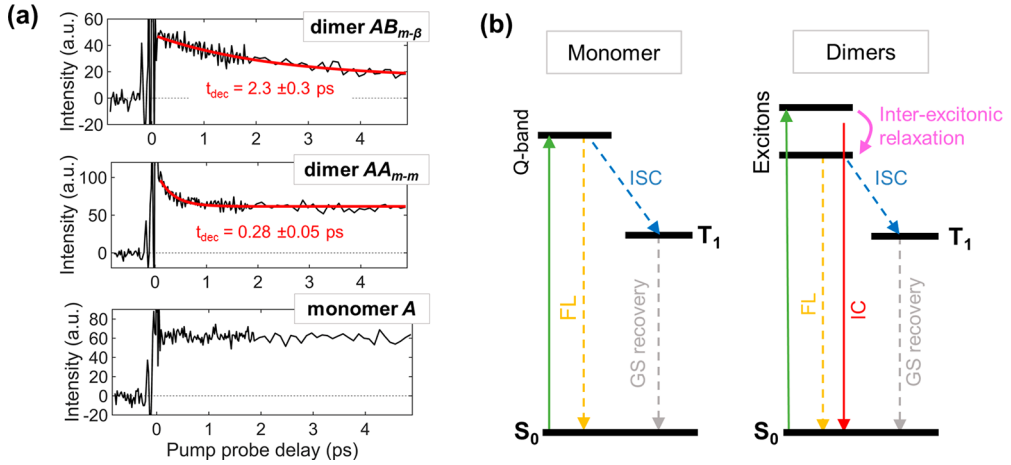

Figure 2. (a) Pump−probe transients of dimers $AB_{m-\beta}$ and AA_{m-m}, along with monomer A measured at 95 K with probe frequency set at ground state bleach maximum. The red line represents the monoexponential fit of the transient discarding the initial ∼80 fs (to avoid any artifact due to pulse overlap). (b) Schematic representation of excitation energy relaxation after Q-band excitation of the monomer and dimers. The upward green arrows represent the excitation. The solid and dotted downward arrows represent the fast (∼ps) and slow (>ns) relaxation channels, respectively. The relaxation pathways of intersystem crossing (ISC), fluorescence (FL), slow ground state (GS) recovery, fast ground state recovery by internal conversion (IC), and interexcitonic relaxation are shown by blue, yellow, gray, red and pink arrows, respectively.

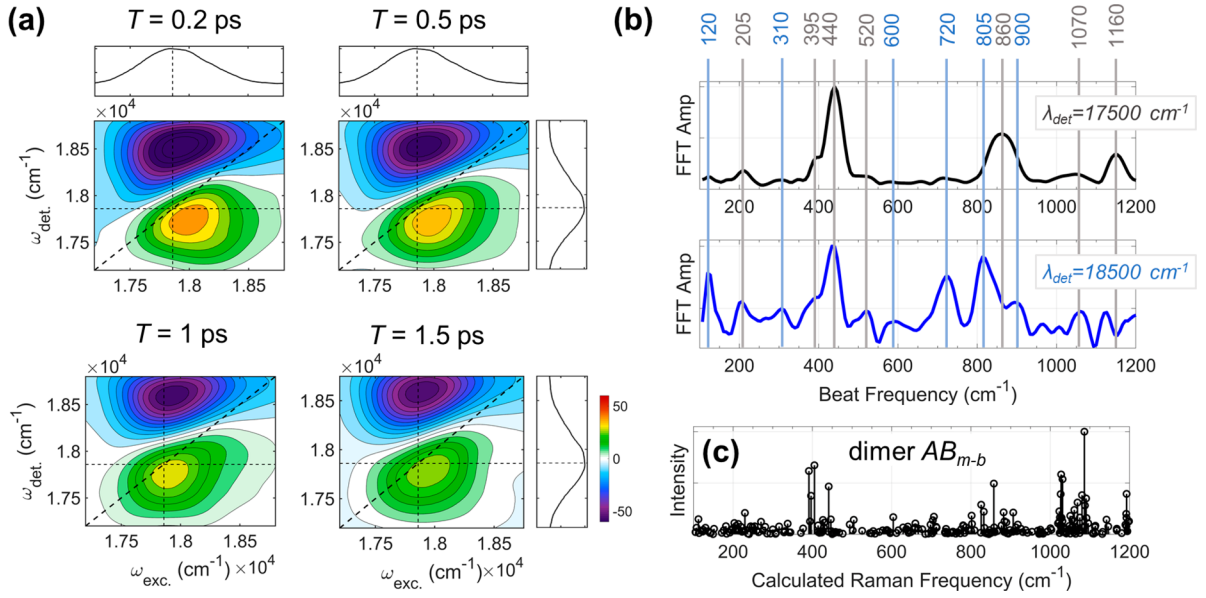

Figure 3. (a) Two-dimensional electronic spectra (2DES) spectra of the dimer $AB_{m-\beta}$ at a few selected waiting times (T) in the detection frequency range from 17 200 to 18 800 cm^{-1} measured at 95 K. The linear absorption spectra are shown on the top and right panels for reference. (b) Coherence beat frequencies obtained by Fourier transforming the set of 2DES data along the waiting time and integrating over the excitation frequency axis at two different detection frequencies: 17 500 (black) and 18 500 (blue) cm^{-1}. (c) The calculated Raman spectrum for the optimized geometry in the ground state of the $AB_{m-\beta}$ dimer.

One- and Two-Dimensional Optical Spectroscopy. *Comparison of Exciton Dynamics.* Pump−probe transients (see experimental methods in the Supporting Information) for the two dimers and for monomer A, excited in the higher frequency Q-band region, are shown in Figure 2a with the probe wavelength set to the maximum of the ground state bleach (GSB) at 95 K. On the 5 ps time scale of the measurements, monomer A shows no decay, while the dimers show a fast decay indicating rapid repopulation of the ground state. The initial decay of the AA_{m-m} dimer (0.28 ± 0.05 ps) is eight times faster than that of the $AB_{m-\beta}$ dimer (2.3 ± 0.3 ps). In both dimers the initial decay of the pump−probe signal is followed by a constant finite value at a later time indicating a partial recovery of the ground state population. We also measured the fluorescence lifetimes at 95 K by time-correlated single-photon counting. The decay times were 2.71 ns (A), 2.43 ns ($AB_{m-\beta}$), and 2.83 ns (AA_{m-m}).

The photophysics of monomeric zinc porphyrin compounds is well established.[58−62] The Q-state of the monomer exhibits intersystem crossing to a triplet state on the ns time scale. The triplet state subsequently decays to S_0 on the μs time scale (Figure 2b). For the dimers, an additional fast (ps) component contributes to their dynamics. In a previous study of porphyrin dimers, it was proposed that these systems undergo rapid nonradiative internal conversion (IC) to S_0 during conformational relaxation on the S_1 surface.[63,64] This phenomenon of

https://doi.org/10.1021/jacs.1c12889
J. Am. Chem. Soc. 2022, 144, 6298−6310

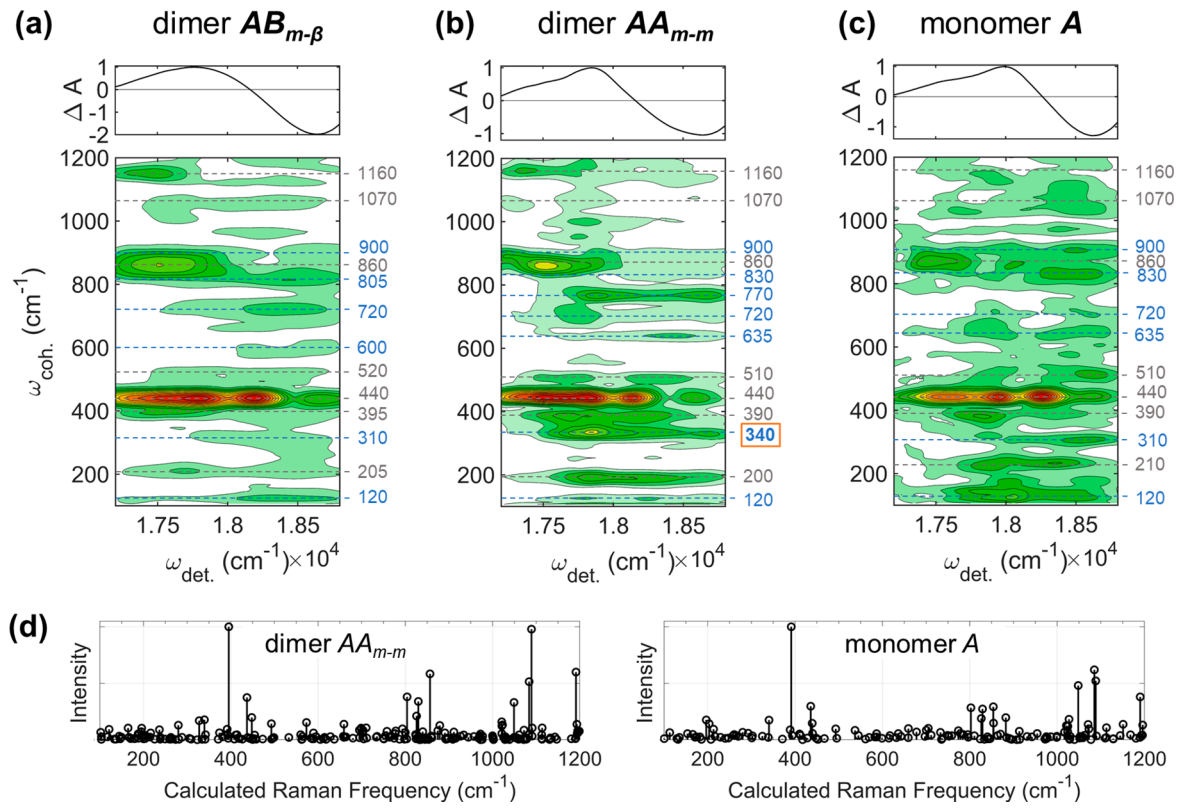

Figure 4. Coherence beat frequencies of (a) dimer $AB_{m-\beta}$, (b) dimer AA_{m-m}, and (c) monomer A obtained by Fourier transforming along the waiting time axis and integrating over the excitation frequency axis. The ground and excited state frequencies are denoted with gray and blue, respectively. The upper panel of each 2D graph represents pump−probe transient spectra at 1 ps, indicating the GSB and ESA regions. (d) DFT calculated Raman spectra for the optimized geometry in the ground state of the $AB_{m-\beta}$ dimer and monomer A.

rapid nonradiative IC to S_0 is commonly found in coupled molecular aggregates, and the rate depends strongly on the excitonic interaction.[65−67] Motivated by these dynamics, we propose the kinetic model shown in Figure 2b. We attribute the fast time constants (2.3 ps for dimer $AB_{m-\beta}$ and 0.28 ps for dimer AA_{m-m}) to the ultrafast nonradiative relaxation to S_0. On the other hand, the decay to a constant value (Figure 2a) suggests that there is a competing fast (∼ps) relaxation pathway, which prevents full recovery of the ground state population. We attribute this competing pathway to interexcitonic relaxation combined with conformational relaxation in the dimer.

Two-Dimensional Electronic Spectroscopy. To understand the effect of differential electronic interaction on the coherent dynamics of the dimers, we employed 2DES. The 2DES spectra were recorded for each sample at 95 K with waiting times varying from 0.05 to 1.5 ps and time steps of 10 fs. Figure 3a shows 2DES spectra of dimer $AB_{m-\beta}$ at four waiting times, T = 0.2, 0.5, 1, and 1.5 ps. A GSB band, illustrated by red, appears in the lower (<18 000 cm^{-1}) detection frequency range, while a strong excited-state absorption (ESA) band, illustrated in purple, appears at higher (>18 000 cm^{-1}) detection frequencies. The intensities of the GSB as well as the ESA bands decay with increasing waiting time, in agreement with our pump−probe data. On top of the monoexponential population decay of the 2DES transient, a number of coherent oscillations were observed. After subtracting the population decay and Fourier transforming the oscillatory residuals, beat frequencies were obtained (Figure 3b). Since there is significant overlap of the ESA and GSB bands, the coherent oscillations that arise from the ground and excited electronic manifolds are expected to overlap. However, we can distinguish the ground and excited state features qualitatively by comparing two extreme detection frequencies at the edges of the spectra, 17 500 and 18 500 cm^{-1}, which are dominated by the GSB and ESA signals, respectively. The beating frequencies of 205, 395, 440, 520, 860, 1070, and 1160 cm^{-1} were found to be present at ω_{det} = 17 500 and 18 500 cm^{-1}. Thus, they are most likely active in both ground and excited electronic manifolds. All of these frequencies match the calculated ground state Raman frequencies (Figure 3c). At ω_{det} = 18 500 cm^{-1}, additional beat frequencies: 120, 310, 600, 720, 805, and 900 cm^{-1} are found to be present and thus are assigned to the excited electronic states.

Figure 4a, b, and c illustrate the coherence beat frequencies at all detection frequencies for the dimers $AB_{m-\beta}$, AA_{m-m} and the control monomer A. The map is obtained by Fourier transforming the 3D data set (ω_{exc}, T, ω_{det}) along the waiting time axis (T) and integrating over the excitation frequency axis (ω_{exc}). The top panel in each graph represents the pump−probe transient spectra at 1 ps, indicating the detection frequencies dominated by GSB and ESA. Following the same analysis of differentiating two different detection frequency regions and comparing with the calculated ground state Raman spectrum of the corresponding sample (Figure 4d), we assign the beat frequencies to the ground and excited electronic manifolds in each sample. For the dimer AA_{m-m}, the beat frequencies at 200, 390, 440, 510, 860, 1070, and 1160 cm^{-1} are assigned to both ground and excited states, whereas those

https://doi.org/10.1021/jacs.1c12889
J. Am. Chem. Soc. 2022, 144, 6298−6310

at 120, 340, 635, 720, 770, 830, and 900 cm^{-1} are assigned mainly to the excited states. For the control monomer *A*, the beat frequencies at 210, 390, 440, 510, 860, 1070, and 1160 cm^{-1} are assigned to both ground and excited states, while those at 120, 310, 635, 720, 830, and 900 cm^{-1} are assigned mainly to the excited states. Comparing the coherence beat frequencies of these three compounds, we see that most of the beat frequencies, especially those belonging to the ground state, appear to be almost identical for all of the samples. This finding indicates negligible perturbation of the ground state vibrational structure when two monomers are closely packed by the 1,2-phenylene linker in the cofacial $AB_{m\text{-}\beta}$ and $AA_{m\text{-}m}$ dimers.

Characterization of the Coherences. Although we have assigned the beat frequencies of the dimer to ground and excited electronic manifolds, quantum beating in 2D spectra can arise from any coherence between the vibrational states or the electronic states, or coherences between vibronic states of mixed character. A hint about the characteristics of these beats can be obtained by comparing the set of frequencies observed for the dimers with the control monomer and the calculated ground state Raman spectrum as follows. If we compare dimer $AA_{m\text{-}m}$ and monomer *A*, most of the frequencies appear to be the same (±5 cm^{-1}). However, contrast in beat frequencies is observed in the region around 300 cm^{-1}. The beat frequency at 310 cm^{-1} in the monomer *A* shifts to 340 cm^{-1} in the dimer $AA_{m\text{-}m}$ and, in addition, a relative increase in intensity is observed, along with a very weak shoulder at 290 cm^{-1}. The frequencies that are common between the monomer and dimer can be characterized as vibrational. On the other hand, frequencies that differ between monomer and dimer could result from either (i) a perturbation in chemical structure by formation of the dimer, causing a slight modification of the excited state potential and thus leading to a shift in vibrational frequencies, or (ii) vibronic coupling between a pair of excitons and a particular vibrational mode. One way to distinguish the vibrational and electronic/vibronic coherence clearly is to compare the coherence beat map patterns obtained from rephasing and nonrephasing pathways. Generally, an electronic/vibronic coherence contributes to an off-diagonal position on the rephasing map and a diagonal position on the nonrephasing map, while a purely vibrational coherence contributes to diagonal and off-diagonal positions on both rephasing and nonrephasing maps.[68] The beat frequency at 340 cm^{-1} in the $AA_{m\text{-}m}$ dimer contributes predominantly to an off-diagonal position on the rephasing map but predominantly to a diagonal position on the nonrephasing map (Figure 5a). This is in contrast to the beat map pattern of the ground state vibrational coherence at 440 cm^{-1} (Figure 5b), which appears in both diagonal and off-diagonal positions on the rephasing and nonrephasing maps, as expected for a purely vibrational coherence. It was not possible to extract the decoherence time by fitting following spectral filtering, due to the congestion of the multiple beating modes in the low frequency region. However, a sliding window FFT analysis gives a decoherence time of 340 cm^{-1} (0.8 ± 0.3 ps), slightly shorter than of 440 cm^{-1} (1.1 ± 0.3 ps). Considering all of these signatures, we characterize the 340 cm^{-1} beating as a vibronic coherence. Further support comes from the calculated Raman modes, which indicate the presence of an out-of-plane porphyrin ring torsional mode at 308 cm^{-1} in the dimer (Figure 5c). An out-of-plane mode of this kind can modulate the interplane separation between the connected porphyrin rings, thus

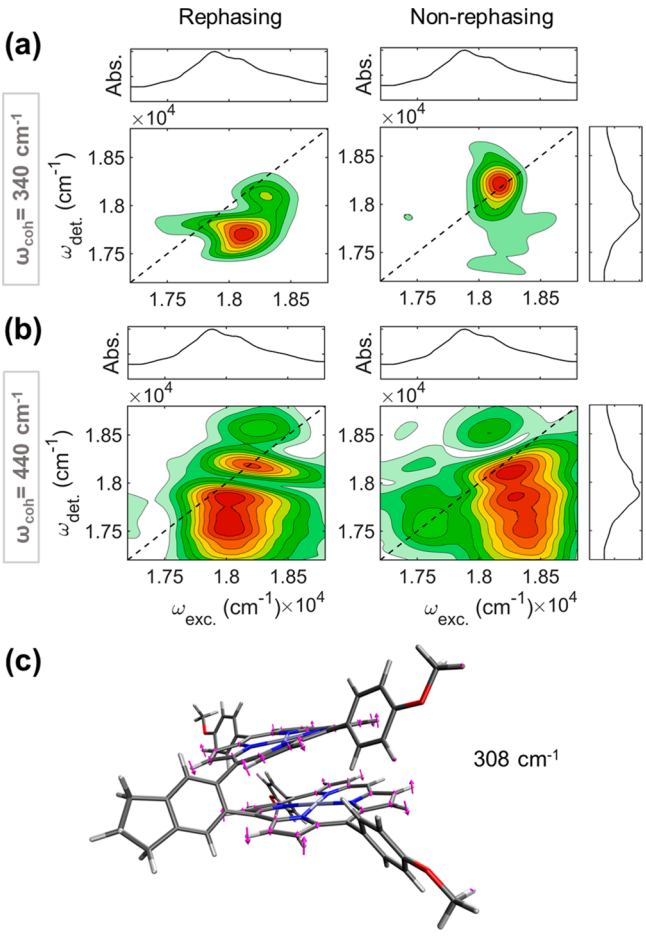

Figure 5. 2D beat frequency map of the dimer $AA_{m\text{-}m}$ at two different beating frequencies (ω_{coh}), (a) 340 cm^{-1} and (b) 440 cm^{-1}. The left 2D graphs show the beating map from rephasing pathways, whereas the right 2D graphs show the beating map from nonrephasing pathways. The linear absorption spectrum is shown in the top and right panels. (c) DFT calculated out-of-plane torsional mode at 308 cm^{-1}.

regulating the electronic coupling between the excitonic states. Hence, we suggest that this mode couples to one of the delocalized excitonic pairs in the dimer $AA_{m\text{-}m}$ and gives rise to vibronic activity. This raises the question whether or not this vibronic coupling plays a role in the acceleration of the exciton dynamics in dimer $AA_{m\text{-}m}$ compared to dimer $AB_{m\text{-}\beta}$, which lacks this vibronic activity. This question has been addressed by theoretical analysis described in the next section.

Model and Exciton-Vibration Dynamics. *Two-State Exciton Model.* We developed a simple model to understand the exciton dynamics observed in the pump−probe experiments. As discussed earlier, the DFT calculations suggest that there is significant oscillator strength for excitation to the S_1 and S_3 states in the case of the $AA_{m\text{-}m}$ dimer, and to state S_3 in the case of the $AB_{m\text{-}\beta}$ dimer, with smaller oscillator strength linked to other states in both cases (Figure 1c). While the computed oscillator strength does not include vibrational components, the intensities of the peak splittings in the experimental absorption spectra suggest that the pump laser excites the S_1 and S_3 states in the case of the homodimer $AA_{m\text{-}m}$, with approximately equal coefficients, while only the S_3 state is excited in the case of the heterodimer $AB_{m\text{-}\beta}$ (Figure 1c).

https://doi.org/10.1021/jacs.1c12889
J. Am. Chem. Soc. 2022, 144, 6298−6310

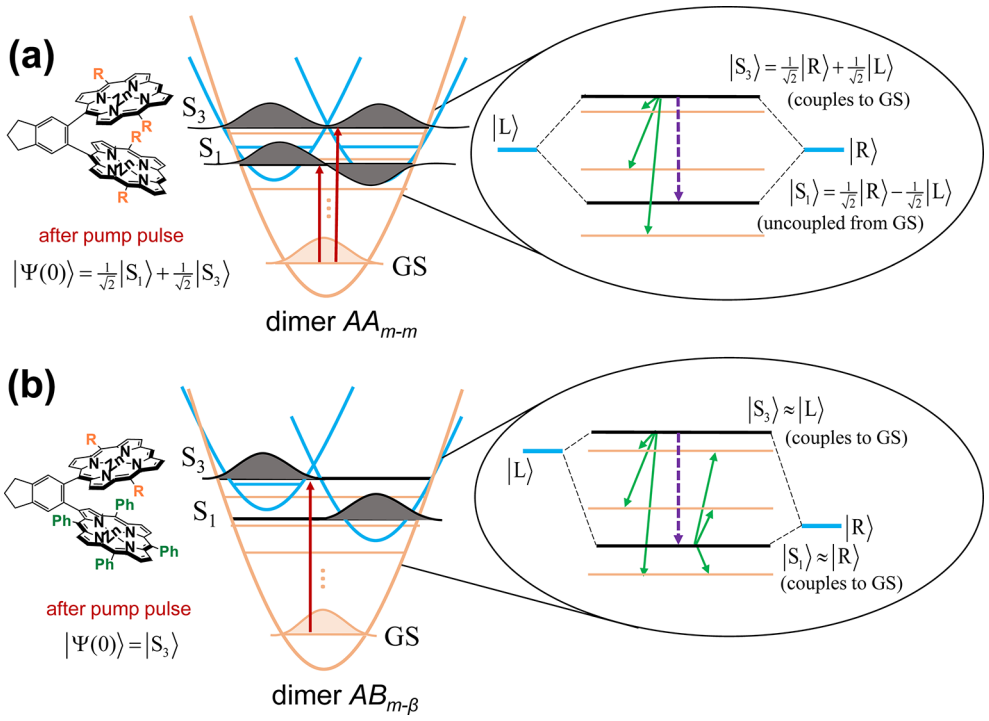

Figure 6. Schematic illustration (not drawn to scale) of the exciton diabatic potential surfaces and the electronic ground state (GS) with a few vibrational gateway states for nonradiative relaxation for (a) dimer $AA_{m\text{-}m}$ and (b) dimer $AB_{m\text{-}\beta}$. Because of wave function symmetry, the lower exciton (S_1) does not couple to the GS in the homodimer ($AA_{m\text{-}m}$). In the heterodimer ($AB_{m\text{-}\beta}$) both excitons are assumed to couple to the GS equally. The respective states excited by the pump pulse are shown on the left. The purple and green arrows represent the excitonic relaxation (ER) and GS recovery pathways, respectively.

The model Hamiltonian includes the electronic ground state and the two exciton states, S_1 and S_3. In the case of the symmetric homodimer, we construct "localized" states from sum and difference combinations of the two exciton eigenstates (see Figure 6). Within the simplified two-state model for the dimer excited states, the two localized states couple equally to S_0 and their difference (the lower exciton S_1) does not couple to the ground state. As discussed earlier, the linear absorption spectrum suggests a splitting of the exciton pair in the $AA_{m\text{-}m}$ dimer of approximately 200 cm^{-1}, which corresponds to an electronic coupling value V_{13} = 100 cm^{-1} (which is considerably smaller than the coupling obtained from the DFT calculations, namely V_{13} = 395 cm^{-1}). Our dynamical calculations on the homodimer $AA_{m\text{-}m}$ with the value V_{13} = 100 cm^{-1} produced good agreement with the time dependence of the ground state recovery obtained in the pump−probe study. According to Table 2, the coupling in the heterodimer is smaller by approximately a factor of 3. We obtained better agreement with the pump−probe experiments using the coupling value V_{13} = 20 cm^{-1} for the $AB_{m\text{-}\beta}$ dimer, along with an energy asymmetry in the diabatic states, which reflects the different excitation energies of the *A* and *B* monomers.

As discussed in the above and verified by the electronic structure analysis of the metalloporphyrin monomers, the absence of the 0−2 and higher transitions indicates that the vibrational modes (with the possible exception of the 310 cm^{-1} mode, which is discussed later) have very small Huang−Rhys factors, while the large intensity of the 0−1 peaks suggests that (at least in the case of high frequency modes) these transitions arise almost exclusively from HT contributions. TDDFT calculations on unsubstituted zinc-porphyrin compounds[36] obtained a difference of vertical transition energies of about 0.03 eV (approximately 240 cm^{-1}), which corresponds to a total vibrational reorganization energy of 120 cm^{-1}.

The high-frequency molecular modes in the 600−1500 cm^{-1} range, which comprise the 0−1 band, were found[36] to couple very weakly to the electronic states of metalloporphyrin monomers. The similarity of the Q-bands between dimers and monomer suggests that the high-frequency modes couple weakly to the electronic states in the dimers as well. Thus, their main effect on the exciton dynamics is a small renormalization of the electronic coupling. From fluorescence spectra (Figure S1), we determined the solvent Stokes shift to be 140−180 cm^{-1}, from which we infer that the solvent reorganization energy is 70−90 cm^{-1}.

Inclusion of 310 cm^{-1} Vibrational Mode. Based on the above considerations, we explicitly include the 310 cm^{-1} vibrational mode in the Hamiltonians for both dimers, while treating all other molecular and solvent modes using a model spectral density with a maximum at 300 cm^{-1} and a total (vibrational and solvent) reorganization energy equal to 200 cm^{-1}. Even though each of the two monomeric units has its own 310 cm^{-1} mode, only the anticorrelated linear combination of these two modes couples to the exciton states.[69] While the two monomer modes can be treated explicitly in the path integral calculations and the two-mode vibrational density can exhibit nontrivial evolution,[70] inclusion of the single anticorrelated common mode allows easier visualization without altering the electronic populations. We note that the 310 cm^{-1} mode does not couple directly to the bath modes. Further, to account for the nonradiative relaxation, three highly excited vibrational states of the electronic ground state, which are near-resonant with the exciton states, are included explicitly in the Hamiltonian. The

https://doi.org/10.1021/jacs.1c12889
J. Am. Chem. Soc. 2022, 144, 6298−6310

ground state potential surface is expected to be strongly anharmonic in this energy range. The role of these gateway states is simply to facilitate electronic population transfer to the S_0 state. The parameters characterizing the gateway states were optimized to generate results similar to those obtained in the pump–probe spectra. A diagrammatic illustration of the diabatic potentials and states is given in Figure 6.

The vibronic character of the 310 cm^{-1} mode suggests that this mode couples more strongly than most other vibrational modes to the $AA_{m\text{-}m}$ excited states, causing a vibronic frequency shift to 340 cm^{-1}, while no frequency shift is observed in the case of $AB_{m\text{-}\beta}$. Explicitly including this mode in the model Hamiltonian with a Huang–Rhys factor of 0.1, we are able to reproduce the observed vibronic shift in $AA_{m\text{-}m}$, while with the same Huang–Rhys factor this mode does not cause vibronic effects on $AB_{m\text{-}\beta}$. Figure 7 shows the eigenvalues

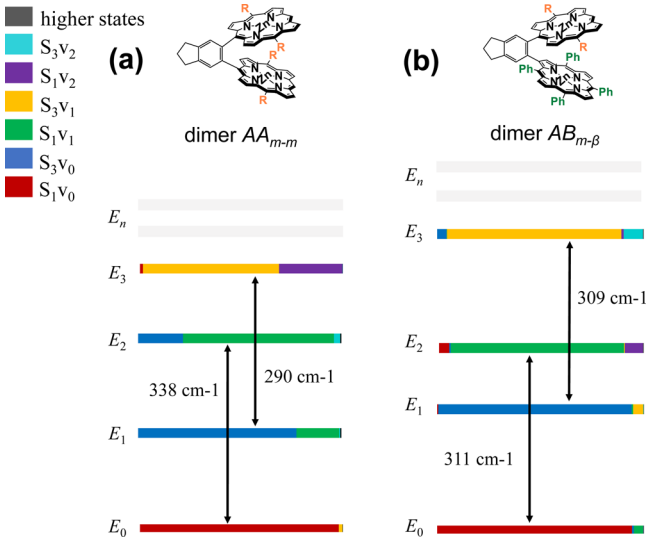

Figure 7. Vibronic eigenstates arising from the coupling of the 310 cm^{-1} mode to the S_1 and S_3 states of the two dimers. The contributions from electronic and vibrational product states are shown in different colors. The modified vibrational energy gaps are indicated.

and the vibronic characters of the four lowest eigenstates obtained with these parameters. The eigenstates are found to be strongly mixed in the $AA_{m\text{-}m}$ case. The two eigenstates with mainly S_1 character are separated by a 338 cm^{-1} gap, while the pair of states with mainly S_3 character has a 290 cm^{-1} gap. Both of these frequencies were observed in the coherence beat maps of this dimer. On the other hand, no substantial mixing is observed in the calculated eigenstates of the heterodimer $AB_{m\text{-}\beta}$, in agreement with the experimental findings. The 310 cm^{-1} mode contributes 31 cm^{-1} to the vibrational reorganization energy.

In the case of the $AA_{m\text{-}m}$ dimer, the exciton eigenstates are delocalized. With the assumption of approximately equal oscillator strengths to the S_1 and S_3 states, excitation by the pump pulse prepares a superposition of these two states, which is primarily localized (see Figure 6). In the case of dimer $AB_{m\text{-}\beta}$, whose eigenstates are localized, excitation to the S_3 state produces a localized state as well. The solvent modes are assumed to be in thermal equilibrium with respect to the ground electronic state. The calculations were carried out at the experimental temperature of 95 K.

Comparison of Exciton Dynamics. The time evolution of the electronic density matrix at 95 K, from which exciton populations and coherences were obtained, was calculated using the numerically exact, fully quantum mechanical small matrix path integral (SMatPI)[26,27] methodology. The SMatPI algorithm is based on an exact decomposition of the quasi-adiabatic propagator path integral (QuAPI)[25] that eliminates tensor storage, yet fully accounts for the entanglement of path integral variables within the memory length. The SMatPI decomposition employs only matrices of minimal size, which is equal to that of the reduced density matrix of the electronic system, thus allowing the treatment of multistate Hamiltonians and long-memory processes. The fully quantum mechanical treatment of all vibrational and solvent degrees of freedom in the Hamiltonian, and of their coupling to the electronic states, ensures the accurate description of quantum coherence effects, which play a key role in exciton transfer. Similar fully quantum mechanical calculations in multichromophore aggregates can be performed using the modular decomposition of the path integral,[71] which offers linear scaling with aggregate length. The calculated populations of the two exciton states, along with that of the ground state, are shown in Figure 8. In the symmetric $AA_{m\text{-}m}$ dimer, the competition between rapid exciton dynamics and slow nonradiative relaxation to the ground state gives rise to two time scales in the population transfer to the ground state, which lead to a flattening of the

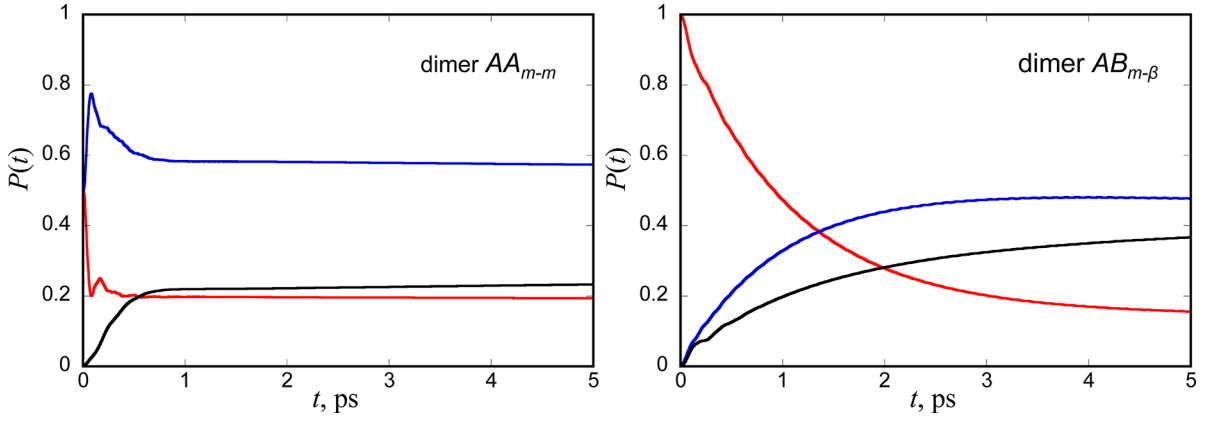

Figure 8. Electronic population dynamics for the dimers $AA_{m\text{-}m}$ (left) and $AB_{m\text{-}\beta}$ (right) from path integral calculations. The red and blue curves show the populations of the S_3 and S_1 states, respectively, while the population of the ground state recovery is shown in black.

https://doi.org/10.1021/jacs.1c12889
J. Am. Chem. Soc. 2022, 144, 6298–6310

ground state recovery curve similar to that observed in the pump−probe experiments. The population of the lower exciton rises very rapidly (∼50 fs) as population is transferred from the higher exciton. At the same time, population is also transferred from S_3 to the ground state on an ∼300 fs time scale. The early time evolution causes the population on the lower exciton (S_1) to rise above the equilibrium value of the two-exciton pair, but is rapidly adjusted as short-lived exciton states die out and the electronic states equilibrate with the bath. The slow leak of population from S_3 to the ground state might be expected to lead to the gradual depletion of this higher exciton state. However, rapid population transfer from the lower exciton to S_3 prevents the depletion of this state, maintaining a constant ratio and thus preserving detailed balance within the exciton pair. These effects lead to population transfer from both excitons to the ground state that is significantly slower than the intraexciton relaxation. In the case of dimer $AB_{m\text{-}\beta}$, the energy difference between the two diabatic states, in combination with the smaller electronic coupling, leads to slower exciton relaxation (∼1 ps) and a gradual rise (∼2 ps) of the ground state population, which gives rise to a typical exponential ground state recovery.

Examination of the time evolution of "coherences" $C_{ij}(t)$, i.e. off-diagonal elements of the reduced density matrix, can uncover further dynamical information regarding the interplay of specific electronic and vibrational time scales. Of particular interest are the coherences of the 310 cm^{-1} mode, which exhibits significant vibronic mixing; thus, i and j denote the vibronic eigenstates shown in Figure 7. For dimer $AA_{m\text{-}m}$ we focus on the coherence $C_{02}(t)$, which corresponds to the frequency characterizing the dominant coherence peak observed experimentally, whereas in the case of $AB_{m\text{-}\beta}$ we report the sum of $C_{02}(t) + C_{13}(t)$ because of the proximity of the two frequencies involved.

Figure 9 shows these coherences for the two dimers. In the case of dimer $AA_{m\text{-}m}$, the coherence oscillates with a period of

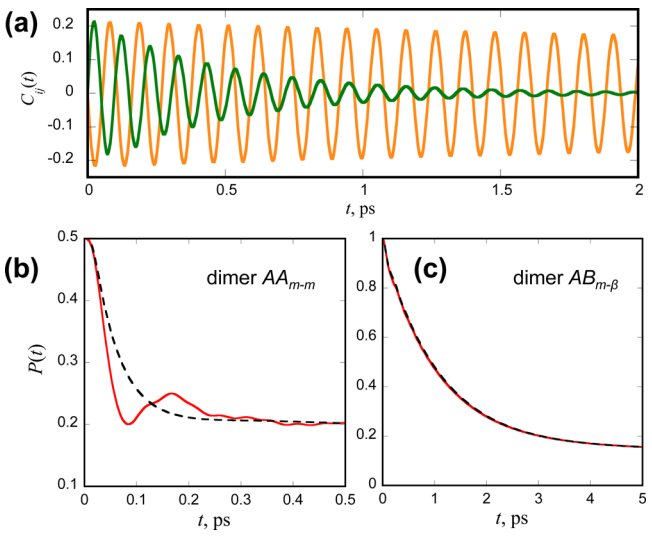

Figure 9. (a) Computed vibronic coherences in the dimers $AA_{m\text{-}m}$ (green) and $AB_{m\text{-}\beta}$ (orange). (b) Population of the higher exciton (S_3) in dimer $AA_{m\text{-}m}$ with (red solid line) and without (black dashed line) the 310 cm^{-1} mode. (c) Same as in b, for dimer $AB_{m\text{-}\beta}$. Note, the time axes in b and c span different ranges to illustrate the effect of vibronic coherence on intraexcitonic relaxation, which proceeds at very different rates for the two dimers.

101 fs, which is equivalent to 330 cm^{-1}, the frequency of the 338 cm^{-1} vibronic energy gap modified by the bath. We therefore characterize this coherence as vibronic, in agreement with the spectroscopic characterization presented in Figure 6. On the other hand, oscillations with a 107 fs period (i.e., 311 cm^{-1}) are observed in the coherence of the dimer $AB_{m\text{-}\beta}$. These oscillations characterize the bare vibrational motion of the excited wavepacket, thereby corroborating the lack of vibronic involvement of the mode in this dimer. Interestingly, the frequency of the vibrational motion is not modified by the THF bath in this case. This is so because the weak mixing with the exciton states leads to less efficient energy exchange with the bath.

A related but interesting feature observed in Figure 9 is the time variation of the coherence amplitudes. The vibronic coherence in the $AA_{m\text{-}m}$ dimer, which characterizes states with a mixed electronic and vibrational character, decays within about 1 ps, in good agreement with the experimental observation. The rapid decay of the coherence is the consequence of indirect coupling (through the exciton states) to the bath of solvent and molecular modes, which enables energy exchange that leads to damping.[72] In sharp contrast, the vibrational coherence in the $AB_{m\text{-}\beta}$ dimer decays on a much longer (∼10 ps) time scale and thus exhibits constant-amplitude oscillations within the 1 ps interval shown in Figure 9a. The smaller electronic coupling (20 cm^{-1} in the $AB_{m\text{-}\beta}$ dimer, compared to 100 cm^{-1} in the $AA_{m\text{-}m}$ dimer) and localized character of the excitons, as illustrated by the very weak mixing of the eigenstates, does not facilitate energy exchange with the bath in this case, leading to the preservation of the vibrational amplitude over very much longer times.

Role of Vibronic Coherence on Exciton Dynamics. Finally, Figure 9b and 9c examine the effect of the vibronic mode on the exciton dynamics. The depletion of the higher exciton is computed to be accelerated by a factor of ∼2 at short times (<100 fs) by vibronic coupling in the $AA_{m\text{-}m}$ dimer. In sharp contrast, coupling to the vibronic mode does not alter the exciton relaxation dynamics in the case of dimer $AB_{m\text{-}\beta}$. The mixing of electronic and vibrational states induced by the 310 cm^{-1} mode provides an additional and highly efficient channel (over and above the effects of the solvent or the bath) for the transfer of population from the higher to the lower exciton. Overall, the effect of stronger exciton coupling facilitated by topology and symmetry as well as vibronic coherence effects makes the dynamics of exciton relaxation almost an order of magnitude faster in dimer $AA_{m\text{-}m}$.

■ CONCLUSIONS

These spectroscopic studies indicate that the metalloporphyrin monomers and dimers have very small total reorganization energies (100−200 cm^{-1}). As with natural light harvesting systems, this means that delocalization and electronic and vibronic coherences can be produced for similarly small electronic couplings. It further follows that significant changes in the excitonic dynamics and the time scales of energy flow can be achieved by rather small changes in molecular topology, as exemplified by the striking difference in the nature and time scales of relaxation for the $AA_{m\text{-}m}$ dimer compared to the $AB_{m\text{-}\beta}$ dimer (which have excitonic couplings that are computed to differ by a factor of 2−3). While the complete and accurate characterization of the electronic structure, exciton-vibration coupling and dipole moment functions of these large systems is beyond the reach of current computational methods, the

https://doi.org/10.1021/jacs.1c12889
J. Am. Chem. Soc. 2022, 144, 6298−6310

simplified model we adopted captured the essential features of the dynamics. The path integral quantum dynamic calculations enable explicit treatment of vibrational degrees of freedom that are functionally important for the transport kinetics and relaxation dynamics in these systems. These quantum dynamics calculations also explain the connection between very rapid exciton transfer between the porphyrins and the slow repopulation of the ground state in the $AA_{m\text{-}m}$ dimer. The simplified model Hamiltonian and the path integral calculations are in excellent agreement with the pump−probe and 2DES dynamics for both dimers. The structural asymmetry of $AB_{m\text{-}\beta}$ produces an excitonic energy offset (~250 cm^{-1}) which, combined with the weaker electronic coupling, is sufficient to destroy the exciton delocalization and coherence. In contrast, the excitons are delocalized in the $AA_{m\text{-}m}$ symmetric dimer. Further, the 2D electronic spectra show evidence for a vibronic coherence in the $AA_{m\text{-}m}$ dimer that is not evident in the $AB_{m\text{-}\beta}$ species. Inclusion of a 310 cm^{-1} mode in the dimer Hamiltonian generates vibronic beats that are shifted to 340 cm^{-1} as a result of vibronic mixing, in agreement with experiment. The calculations show that the vibronic mixing accelerates exciton relaxation by roughly a factor of 2 compared to simulations without this mode. While multiple modes are involved in providing HT intensity to the Q-band transitions,[36] only a single mode appears to be vibronically active in $AA_{m\text{-}m}$. No shift in frequency is found in the $AB_{m\text{-}\beta}$ dimer, and the coherence has the characteristics of a vibrational wavepacket, in agreement with experiment. In the $AB_{m\text{-}\beta}$ dimer, the excitonic relaxation dynamics is much slower and is unaltered by the presence or absence of the 310 cm^{-1} mode.

Fully quantum mechanical calculations of finite-temperature exciton-vibration dynamics in large molecular aggregates are feasible using available real-time path integral methods.[26,27] Recent investigations revealed the rich interplay among exciton transport, coherence-quenching molecular vibrations, and vibronic effects in the dynamics of exciton transport in large chromophore aggregates.[73,74] Optimal design of molecular topology and hence electronic coupling and energy gaps, along with selection of vibrational modes to facilitate electron−nuclear mixing, has the potential to provide a blueprint for rapid and efficient energy transport. The analysis presented here provides a basis for experimental and theoretical studies of larger porphyrin multimers and aggregates[2,75−82] as a path to exploring the optimization and limits of coherence-enabled energy transport.

■ ASSOCIATED CONTENT

Supporting Information

The Supporting Information is available free of charge at https://pubs.acs.org/doi/10.1021/jacs.1c12889.

Sample preparation, Experimental methods, Absorption and Fluorescence spectra, Theoretical calculations, Electronic structure analysis, Natural transition orbitals, Calculations of electronic coupling in different solvents, with different basis sets and methods, and molecular coordinates of optimized ground state geometry. (PDF)

■ AUTHOR INFORMATION

Corresponding Authors

Graham R. Fleming − *Department of Chemistry, University of California, Berkeley, California 94720, United States; Molecular Biophysics and Integrated Bioimaging Division, Lawrence Berkeley National Laboratory, Berkeley, California 94720, United States; Kavli Energy Nanoscience Institute at Berkeley, Berkeley, California 94720, United States;* orcid.org/0000-0003-0847-1838; Email: grfleming@lbl.gov

Nancy Makri − *Department of Chemistry, Department of Physics, and Illinois Quantum Information Science & Technology Center, University of Illinois, Urbana, Illinois 61801, United States;* orcid.org/0000-0002-3310-7328; Email: nmakri@illinois.edu

Authors

Partha Pratim Roy − *Department of Chemistry, University of California, Berkeley, California 94720, United States; Molecular Biophysics and Integrated Bioimaging Division, Lawrence Berkeley National Laboratory, Berkeley, California 94720, United States; Kavli Energy Nanoscience Institute at Berkeley, Berkeley, California 94720, United States;* orcid.org/0000-0003-3202-4333

Sohang Kundu − *Department of Chemistry, University of Illinois, Urbana, Illinois 61801, United States;* orcid.org/0000-0002-5499-9775

Jesús Valdiviezo − *Department of Chemistry and Department of Electrical and Computer Engineering, Duke University, Durham, North Carolina 27708, United States;* orcid.org/0000-0002-8542-1247

George Bullard − *Department of Chemistry, Duke University, Durham, North Carolina 27708, United States;* orcid.org/0000-0002-3725-9046

James T. Fletcher − *Department of Chemistry, University of Pennsylvania, Philadelphia, Pennsylvania 19104, United States;* Present Address: Department of Chemistry, Creighton University, Omaha, NE 68178

Rui Liu − *Department of Chemistry, Duke University, Durham, North Carolina 27708, United States*

Shiun-Jr Yang − *Department of Chemistry, University of California, Berkeley, California 94720, United States; Molecular Biophysics and Integrated Bioimaging Division, Lawrence Berkeley National Laboratory, Berkeley, California 94720, United States*

Peng Zhang − *Department of Chemistry, Duke University, Durham, North Carolina 27708, United States*

David N. Beratan − *Department of Chemistry and Department of Physics, Duke University, Durham, North Carolina 27708, United States; Department of Biochemistry, Duke University, Durham, North Carolina 27710, United States*

Michael J. Therien − *Department of Chemistry, Duke University, Durham, North Carolina 27708, United States;* orcid.org/0000-0003-4876-0036

Complete contact information is available at: https://pubs.acs.org/10.1021/jacs.1c12889

Notes

The authors declare no competing financial interest.

■ ACKNOWLEDGMENTS

The authors acknowledge the Center for Synthesizing Quantum Coherence, supported by the National Science Foundation (CHE-1925690), for funding this research. P.P.R, S.Y., and G.R.F. thank the U.S. Department of Energy, Office of Science, Chemical Sciences, Geosciences, and Biosciences

Division for equipment support and also thank Eric Arsenault and Pallavi Bhattacharyya for helpful discussions. J.V. acknowledges support of a Fulbright-García Robles Scholarship and the Kathleen Zielik Fellowship from Duke University's Department of Chemistry.

REFERENCES

(1) Hestand, N. J.; Spano, F. C. Expanded Theory of H- and J-Molecular Aggregates: The Effects of Vibronic Coupling and Intermolecular Charge Transfer. *Chem. Rev.* **2018**, *118* (15), 7069−7163.
(2) Terazono, Y.; Kodis, G.; Chachisvilis, M.; Cherry, B. R.; Fournier, M.; Moore, A.; Moore, T. A.; Gust, D. Multiporphyrin Arrays with π-π Interchromophore Interactions. *J. Am. Chem. Soc.* **2015**, *137* (1), 245−258.
(3) Sung, J.; Kim, P.; Fimmel, B.; Würthner, F.; Kim, D. Direct Observation of Ultrafast Coherent Exciton Dynamics in Helical π-Stacks of Self-Assembled Perylene Bisimides. *Nat. Commun.* **2015**, *6*, 1−7.
(4) Ishizaki, A.; Calhoun, T. R.; Schlau-Cohen, G. S.; Fleming, G. R. Quantum Coherence and Its Interplay with Protein Environments in Photosynthetic Electronic Energy Transfer. *Phys. Chem. Chem. Phys.* **2010**, *12* (27), 7319−7337.
(5) Chenu, A.; Scholes, G. D. Coherence in Energy Transfer and Photosynthesis. *Annu. Rev. Phys. Chem.* **2015**, *66*, 69−96.
(6) Chenu, A.; Christensson, N.; Kauffmann, H. F.; Mančal, T. Enhancement of Vibronic and Ground-State Vibrational Coherences in 2D Spectra of Photosynthetic Complexes. *Sci. Rep* **2013**, *3*, 1−12.
(7) Proppe, A. H.; Li, Y. C.; Aspuru-Guzik, A.; Berlinguette, C. P.; Chang, C. J.; Cogdell, R.; Doyle, A. G.; Flick, J.; Gabor, N. M.; van Grondelle, R.; et al. Bioinspiration in Light Harvesting and Catalysis. *Nat. Rev. Mater.* **2020**, *5* (11), 828−846.
(8) Brédas, J. L.; Sargent, E. H.; Scholes, G. D. Photovoltaic Concepts Inspired by Coherence Effects in Photosynthetic Systems. *Nat. Mater.* **2017**, *16* (1), 35−44.
(9) Scholes, G. D.; Fleming, G. R.; Chen, L. X.; Aspuru-Guzik, A.; Buchleitner, A.; Coker, D. F.; Engel, G. S.; Van Grondelle, R.; Ishizaki, A.; Jonas, D. M.; et al. Using Coherence to Enhance Function in Chemical and Biophysical Systems. *Nature* **2017**, *543* (7647), 647−656.
(10) Kundu, S.; Makri, N. Intramolecular Vibrations in Excitation Energy Transfer: Insights from Real-Time Path Integral Calculations. *Annu. Rev. Phys. Chem.* **2022**, *73*, 349−375.
(11) Ryu, I. S.; Dong, H.; Fleming, G. R. Role of Electronic-Vibrational Mixing in Enhancing Vibrational Coherences in the Ground Electronic States of Photosynthetic Bacterial Reaction Center. *J. Phys. Chem. B* **2014**, *118* (5), 1381−1388.
(12) Arsenault, E. A.; Yoneda, Y.; Iwai, M.; Niyogi, K. K.; Fleming, G. R. Vibronic Mixing Enables Ultrafast Energy Flow in Light-Harvesting Complex II. *Nat. Commun.* **2020**, *11* (1), 1−8.
(13) Fujihashi, Y.; Fleming, G. R.; Ishizaki, A. Impact of Environmentally Induced Fluctuations on Quantum Mechanically Mixed Electronic and Vibrational Pigment States in Photosynthetic Energy Transfer and 2D Electronic Spectra. *J. Chem. Phys.* **2015**, *142* (21), 212403.
(14) Ishizaki, A.; Fleming, G. R. Unified Treatment of Quantum Coherent and Incoherent Hopping Dynamics in Electronic Energy Transfer: Reduced Hierarchy Equation Approach. *J. Chem. Phys.* **2009**, *130* (23), 234111.
(15) Ishizaki, A.; Fleming, G. R. Quantum Coherence in Photosynthetic Light Harvesting. *Annu. Rev. Condens. Matter Phys.* **2012**, 3 (1), 333−361.
(16) Fletcher, J. T.; Therien, M. J. Extreme Electronic Modulation of the Cofacial Porphyrin Structural Motif. *J. Am. Chem. Soc.* **2002**, *124* (16), 4298−4311.
(17) Fletcher, J. T.; Therien, M. J. Strongly Coupled Porphyrin Arrays Featuring Both π-Cofacial and Linear-π-Conjugative Interactions. *Inorg. Chem.* **2002**, *41* (2), 331−341.
(18) Fletcher, J. T.; Therien, M. J. Transition-Metal-Mediated [2 + 2 + 2]: Cycloaddition Reactions with Ethyne-Containing Porphyrin Templates: New Routes to Cofacial Porphyrin Structures and Facially-Functionalized (Porphinato) Metal Species. *J. Am. Chem. Soc.* **2000**, *122*, 12393−12394.
(19) Hayes, D.; Griffin, G. B.; Engel, G. S. Engineering Coherence Among Excited States in Synthetic Heterodimer Systems. *Science* **2013**, *340*, 1431−1434.
(20) Halpin, A.; Johnson, P. J. M.; Tempelaar, R.; Murphy, R. S.; Knoester, J.; Jansen, T. L. C.; Miller, R. J. D. Two-Dimensional Spectroscopy of a Molecular Dimer Unveils the Effects of Vibronic Coupling on Exciton Coherences. *Nat. Chem.* **2014**, *6* (3), 196−201.
(21) Jumper, C. C.; Anna, J. M.; Stradomska, A.; Schins, J.; Myahkostupov, M.; Prusakova, V.; Oblinsky, D. G.; Castellano, F. N.; Knoester, J.; Scholes, G. D.; et al. Intramolecular Radiationless Transitions Dominate Exciton Relaxation Dynamics. *Chem. Phys. Lett.* **2014**, *599*, 23−33.
(22) Wang, L.; Griffin, G. B.; Zhang, A.; Zhai, F.; Williams, N. E.; Jordan, R. F.; Engel, G. S. Controlling Quantum-Beating Signals in 2D Electronic Spectra by Packing Synthetic Heterodimers on Single-Walled Carbon Nanotubes. *Nat. Chem.* **2017**, *9* (3), 219−225.
(23) Jumper, C. C.; Rafiq, S.; Wang, S.; Scholes, G. D. From Coherent to Vibronic Light Harvesting in Photosynthesis. *Curr. Opin. Chem. Biol.* **2018**, *47*, 39−46.
(24) Dean, J. C.; Scholes, G. D. Coherence Spectroscopy in the Condensed Phase: Insights into Molecular Structure, Environment, and Interactions. *Acc. Chem. Res.* **2017**, *50* (11), 2746−2755.
(25) Makri, N. Quantum Dissipative Dynamics: A Numerically Exact Methodology. *J. Phys. Chem. A* **1998**, *102*, 4414−4427.
(26) Makri, N. Small Matrix Disentanglement of the Path Integral: Overcoming the Exponential Tensor Scaling with Memory Length. *J. Chem. Phys.* **2020**, *152* (4), 041104.
(27) Makri, N. Small Matrix Path Integral for System-Bath Dynamics. *J. Chem. Theory Comput* **2020**, *16* (7), 4038−4049.
(28) Gouterman, M. Spectra Porphyrins. *J. Mol. Spectrosc.* **1961**, *6*, 138−163.
(29) Gouterman, M.; Wagnière, G. H.; Snyder, L. C. Spectra of Porphyrins. Part II. Four Orbital Model. *J. Mol. Spectrosc.* **1963**, *11* (1−6), 108−127.
(30) Small, G. J. Herzberg − Teller Vibronic Coupling and the Duschinsky Effect. *J. Chem. Phys.* **1971**, *54*, 3300.
(31) Czernuszewicz, R. S. Resonance Raman Spectroscopy of Metalloproteins Using CW Laser Excitation. *Spectrosc. Methods Anal* **1993**, *17*, 345−374.
(32) Spiro, T. G.; Czernuszewicz, R. S.; Li, X. Y. Metalloporphyrin Structure and Dynamics from Resonance Raman Spectroscopy. *Coord. Chem. Rev.* **1990**, *100* (C), 541−571.
(33) Santoro, F.; Lami, A.; Improta, R.; Bloino, J.; Barone, V. Effective Method for the Computation of Optical Spectra of Large Molecules at Finite Temperature Including the Duschinsky and Herzberg-Teller Effect: The Qx Band of Porphyrin as a Case Study. *J. Chem. Phys.* **2008**, *128* (22), 224311.
(34) He, R.; Li, H.; Shen, W.; Yang, Q.; Li, M. Vibronic Fine-Structure in the $S_0 \rightarrow S_1$ Absorption Spectrum of Zinc Porphyrin: A Franck-Condon Simulation Incorporating Herzberg-Teller Theory and the Duschinsky Effect. *J. Mol. Spectrosc.* **2012**, *275* (1), 61−70.
(35) Yang, P.; Qi, D.; You, G.; Shen, W.; Li, M.; He, R. Influence of Duschinsky and Herzberg-Teller Effects on $S_0 \rightarrow S_1$ Vibrationally Resolved Absorption Spectra of Several Porphyrin-like Compounds. *J. Chem. Phys.* **2014**, *141* (12), 124304.
(36) Pan, Y.; Li, L.; Qiu, F.; Wei, Y.; Hua, W.; Tian, G. On the Spectral Profile Change in the Q Band Absorption Spectra of Metalloporphyrins (Mg, Zn, and Pd): A First-Principles Study. *J. Chem. Phys.* **2019**, *150* (16), 164308.
(37) Gouterman, M. Study of the Effects of Substitution on the Absorption Spectra of Porphin. *J. Chem. Phys.* **1959**, *30* (5), 1139−1161.

https://doi.org/10.1021/jacs.1c12889
J. Am. Chem. Soc. 2022, 144, 6298−6310

(38) Allouche, A. Software News and Updates Gabedit — A Graphical User Interface for Computational Chemistry Softwares. *J. Comput. Chem.* **2011**, *32*, 174−182.
(39) Yanai, T.; Tew, D. P.; Handy, N. C. A New Hybrid Exchange-Correlation Functional Using the Coulomb-Attenuating Method (CAM-B3LYP). *Chem. Phys. Lett.* **2004**, *393* (1−3), 51−57.
(40) Weigend, F.; Ahlrichs, R. Balanced Basis Sets of Split Valence, Triple Zeta Valence and Quadruple Zeta Valence Quality for H to Rn: Design and Assessment of Accuracy. *Phys. Chem. Chem. Phys.* **2005**, *7* (18), 3297−3305.
(41) Scalmani, G.; Frisch, M. J. Continuous Surface Charge Polarizable Continuum Models of Solvation. I. General Formalism. *J. Chem. Phys.* **2010**, *132* (11), 114110.
(42) Kumble, R.; Palese, S.; Lin, V. S.-Y.; Therien, M. J.; Hochstrasser, R. M. Ultrafast Dynamics of Highly Conjugated Porphyrin Arrays. *J. Am. Chem. Soc.* **1998**, *120* (44), 11489−11498.
(43) Osuka, A.; Nakajima, S.; Nagata, T.; Maruyama, K.; Toriumi, K. A 1,2-Phenylene-Bridged Porphyrin Dimer- Synthesis, Properties, and Molecular Structure. *Angew. Chem., Int. Ed.* **1991**, *30* (5), 582−584.
(44) Naruta, Y.; Sasayama, M.; Sasaki, T. Oxygen Evolution by Oxidation of Water with Manganese Porphyrin Dimers. *Angew. Chem., Int. Ed.* **1994**, *33* (18), 1839−1841.
(45) Frisch, M. J.; Trucks, G. W.; Schlegel, H. B.; Scuseria, G. E.; Robb, M. A.; Cheeseman, J. R.; Scalmani, G.; Barone, V.; Petersson, G. A.; Nakatsuji, H.; Li, X.; Caricato, M.; Marenich, A. V.; Bloino, J.; Janesko, B. G.; Gomperts, R.; Mennucci, B.; Hratch, D. J. No Title. 2016; *Gaussian 16*, Revision A.03; Gaussian Inc.: Wallingford, CT.
(46) Yu, H. S.; He, X.; Li, S. L.; Truhlar, D. G. MN15: A Kohn-Sham Global-Hybrid Exchange-Correlation Density Functional with Broad Accuracy for Multi-Reference and Single-Reference Systems and Noncovalent Interactions. *Chem. Sci.* **2016**, *7* (8), 5032−5051.
(47) Christiansen, O.; Koch, H.; Jørgensen, P. The Second-Order Approximate Coupled Cluster Singles and Doubles Model CC2. *Chem. Phys. Lett.* **1995**, *243* (5−6), 409−418.
(48) Balasubramani, S. G.; Chen, G. P.; Coriani, S.; Diedenhofen, M.; Frank, M. S.; Franzke, Y. J.; Furche, F.; Grotjahn, R.; Harding, M. E.; Hättig, C.; et al. TURBOMOLE: Modular Program Suite for Ab Initio Quantum-Chemical and Condensed-Matter Simulations. *J. Chem. Phys.* **2020**, *152* (18), 184107.
(49) Leszczynski, J. *Handbook of Computational Chemistry*, 2nd ed.; 2017.
(50) Struve, W. S. *Fundamentals of Molecular Spectroscopy*; John Wiley & Sons: New York, 1989.
(51) Arsenault, E. A.; Schile, A. J.; Limmer, D. T.; Fleming, G. R. Vibronic Coupling in Energy Transfer Dynamics and Two-Dimensional Electronic-Vibrational Spectra. *J. Chem. Phys.* **2021**, *155* (5), 054201.
(52) Zhang, H. D.; Qiao, Q.; Xu, R. X.; Yan, Y. Effects of Herzberg-Teller Vibronic Coupling on Coherent Excitation Energy Transfer. *J. Chem. Phys.* **2016**, *145* (20), 204109.
(53) Craig, D. F.; Small, G. J. Totally Symmetric Vibronic Perturbations and the Phenanthrene 3400-Å Spectrum. *J. Chem. Phys.* **1969**, *50* (9), 3827−3834.
(54) Shao, Y.; Gan, Z.; Epifanovsky, E.; Gilbert, A. T. B.; Wormit, M.; Kussmann, J.; Lange, A. W.; Behn, A.; Deng, J.; Feng, X.; et al. Advances in Molecular Quantum Chemistry Contained in the Q-Chem 4 Program Package. *Mol. Phys.* **2015**, *113* (2), 184−215.
(55) You, Z. Q.; Hsu, C. P. Theory and Calculation for the Electronic Coupling in Excitation Energy Transfer. *Int. J. Quantum Chem.* **2014**, *114* (2), 102−115.
(56) Hsu, C. P.; You, Z. Q.; Chen, H. C. Characterization of the Short-Range Couplings in Excitation Energy Transfer. *J. Phys. Chem. C* **2008**, *112* (4), 1204−1212.
(57) Zheng, J.; Kang, Y. K.; Therien, M. J.; Beratan, D. N. Generalized Mulliken-Hush Analysis of Electronic Coupling Interactions in Compressed π-Stacked Porphyrin-Bridge-Quinone Systems. *J. Am. Chem. Soc.* **2005**, *127* (32), 11303−11310.
(58) Kullmann, M.; Hipke, A.; Nuernberger, P.; Bruhn, T.; Götz, D. C. G.; Sekita, M.; Guldi, D. M.; Bringmann, G.; Brixner, T. Ultrafast Exciton Dynamics after Soret- or Q-Band Excitation of a Directly β,β′-Linked Bisporphyrin. *Phys. Chem. Chem. Phys.* **2012**, *14* (22), 8038−8050.
(59) Verma, S.; Ghosh, A.; Das, A.; Ghosh, H. N. Ultrafast Exciton Dynamics of J- and H-Aggregates of the Porphyrin-Catechol in Aqueous Solution. *J. Phys. Chem. B* **2010**, *114* (25), 8327−8334.
(60) Liu, X.; Tripathy, U.; Bhosale, S. V.; Langford, S. J.; Steer, R. P. Photophysics of Soret-Excited Tetrapyrroles in Solution. II. Effects of Perdeuteration, Substituent Nature and Position, and Macrocycle Structure and Conformation in Zinc(II) Porphyrins. *J. Phys. Chem. A* **2008**, *112* (38), 8986−8998.
(61) Koch, F.; Kullmann, M.; Selig, U.; Nuernberger, P.; Götz, D. C. G.; Bringmann, G.; Brixner, T. Coherent Two-Dimensional Electronic Spectroscopy in the Soret Band of a Chiral Porphyrin Dimer. *New J. Phys.* **2013**, *15*, 025006.
(62) Venkatesh, Y.; Venkatesan, M.; Ramakrishna, B.; Bangal, P. R. Ultrafast Time-Resolved Emission and Absorption Spectra of Meso-Pyridyl Porphyrins upon Soret Band Excitation Studied by Fluorescence Up-Conversion and Transient Absorption Spectroscopy. *J. Phys. Chem. B* **2016**, *120* (35), 9410−9421.
(63) Cho, H. S.; Song, N. W.; Kim, Y. H.; Jeoung, S. C.; Hahn, S.; Kim, D.; Kim, S. K.; Yoshida, N.; Osuka, A. Ultrafast Energy Relaxation Dynamics of Directly Linked Porphyrin Arrays. *J. Phys. Chem. A* **2000**, *104* (15), 3287−3298.
(64) Moretti, L.; Kudisch, B.; Terazono, Y.; Moore, A. L.; Moore, T. A.; Gust, D.; Cerullo, G.; Scholes, G. D.; Maiuri, M. Ultrafast Dynamics of Nonrigid Zinc-Porphyrin Arrays Mimicking the Photosynthetic "Special Pair". *J. Phys. Chem. Lett.* **2020**, *11* (9), 3443−3450.
(65) Dean, J. C.; Oblinsky, D. G.; Rafiq, S.; Scholes, G. D. Methylene Blue Exciton States Steer Nonradiative Relaxation: Ultrafast Spectroscopy of Methylene Blue Dimer. *J. Phys. Chem. B* **2016**, *120* (3), 440−454.
(66) Caplins, B. W.; Mullenbach, T. K.; Holmes, R. J.; Blank, D. A. Intermolecular Interactions Determine Exciton Lifetimes in Neat Films and Solid State Solutions of Metal-Free Phthalocyanine. *J. Phys. Chem. C* **2015**, *119* (49), 27340−27347.
(67) Huff, J. S.; Davis, P. H.; Christy, A.; Kellis, D. L.; Kandadai, N.; Toa, Z. S. D.; Scholes, G. D.; Yurke, B.; Knowlton, W. B.; Pensack, R. D. DNA-Templated Aggregates of Strongly Coupled Cyanine Dyes: Nonradiative Decay Governs Exciton Lifetimes. *J. Phys. Chem. Lett.* **2019**, *10* (10), 2386−2392.
(68) Butkus, V.; Zigmantas, D.; Valkunas, L.; Abramavicius, D. Vibrational vs. Electronic Coherences in 2D Spectrum of Molecular Systems. *Chem. Phys. Lett.* **2012**, *545*, 40−43.
(69) Piepho, S. B.; Krausz, E. R.; Schatz, P. N. Vibronic Coupling Model for Calculation of Mixed Valence Absorption Profiles. *J. Am. Chem. Soc.* **1978**, *100* (10), 2996−3005.
(70) Kundu, S.; Makri, N. Electronic-Vibrational Density Evolution in a Perylene Bisimide Dimer: Mechanistic Insights into Excitation Energy Transfer. *Phys. Chem. Chem. Phys.* **2021**, *23* (29), 15503−15514.
(71) Makri, N. Modular Path Integral Methodology for Real-Time Quantum Dynamics. *J. Chem. Phys.* **2018**, *149* (21), 214108.
(72) Kundu, S.; Makri, N. Time Evolution of Bath Properties in Spin-Boson Dynamics. *J. Phys. Chem. B* **2021**, *125* (29), 8137−8151.
(73) Kundu, S.; Makri, N. Real-Time Path Integral Simulation of Exciton-Vibration Dynamics in Light-Harvesting Bacteriochlorophyll Aggregates. *J. Phys. Chem. Lett.* **2020**, *11* (20), 8783−8789.
(74) Kundu, S.; Makri, N. Origin of Vibrational Features in the Excitation Energy Transfer Dynamics of Perylene Bisimide J-Aggregates. *J. Chem. Phys.* **2021**, *154* (11), 114301.
(75) Peterson, E. J.; Qi, W.; Stanton, I. N.; Zhang, P.; Therien, M. J. Driving High Quantum Yield NIR Emission through Proquinoidal Linkage Motifs in Conjugated Supermolecular Arrays. *Chem. Sci.* **2020**, *11* (31), 8095−8104.
(76) Tanaka, T.; Osuka, A. Conjugated Porphyrin Arrays: Synthesis, Properties and Applications for Functional Materials. *Chem. Soc. Rev.* **2015**, *44* (4), 943−969.

https://doi.org/10.1021/jacs.1c12889
J. Am. Chem. Soc. 2022, 144, 6298−6310

(77) Parkinson, P.; Knappke, C. E. I.; Kamonsutthipaijit, N.; Sirithip, K.; Matichak, J. D.; Anderson, H. L.; Herz, L. M. Ultrafast Energy Transfer in Biomimetic Multistrand Nanorings. *J. Am. Chem. Soc.* **2014**, *136* (23), 8217−8220.
(78) O'Sullivan, M. C.; Sprafke, J. K.; Kondratuk, D. V.; Rinfray, C.; Claridge, T. D. W.; Saywell, A.; Blunt, M. O.; O'Shea, J. N.; Beton, P. H.; Malfois, M.; et al. Vernier Templating and Synthesis of a 12-Porphyrin Nano-Ring. *Nature* **2011**, *469* (7328), 72−75.
(79) Duncan, T. V.; Susumu, K.; Sinks, L. E.; Therien, M. J. Exceptional Near-Infrared Fluorescence Quantum Yields and Excited-State Absorptivity of Highly Conjugated Porphyrin Arrays. *J. Am. Chem. Soc.* **2006**, *128* (28), 9000−9001.
(80) Rubtsov, I. V.; Susumu, K.; Rubtsov, G. I.; Therien, M. J. Ultrafast Singlet Excited-State Polarization in Electronically Asymmetric Ethyne-Bridged Bis[(Porphinato)Zinc(II)] Complexes. *J. Am. Chem. Soc.* **2003**, *125* (9), 2687−2696.
(81) Li, J.; Ambroise, A.; Yang, S. I.; Diers, J. R.; Seth, J.; Wack, C. R.; Bocian, D. F.; Holten, D.; Lindsey, J. S. Template-Directed Synthesis, Excited-State Photodynamics, and Electronic Communication in a Hexameric Wheel of Porphyrins. *J. Am. Chem. Soc.* **1999**, *121* (38), 8927−8940.
(82) Lin, V. S.-Y.; DiMagno, S. G.; Therien, M. J. Highly Conjugated, Acetylenyl Bridged Porphyrins: New Models for Light-Harvesting Antenna Systems. *Science* **1994**, *264* (5162), 1105−1111.

https://doi.org/10.1021/jacs.1c12889
J. Am. Chem. Soc. 2022, 144, 6298−6310